AGU PUBLICATIONS

JGR

Journal of Geophysical Research: Space Physics

RESEARCH ARTICLE
10.1002/2016JA023318

How is the Jovian main auroral emission affected by the solar wind?

E. Chané[1], J. Saur[2], R. Keppens[1], and S. Poedts[1]

[1]Centre for mathematical Plasma Astrophysics, KU Leuven, Celestijnenlaan, Belgium, [2]Institut für Geophysik und Meteorologie, Universität zu Köln, Albertus-Magnus-Platz, Germany

Key Points:
- The solar wind ram pressure and the brightness of the main oval are positively correlated at Jupiter
- Local time asymmetries in the magnetosphere are enhanced when the solar wind ram pressure increases
- The main oval becomes broader at noon local time when the solar wind ram pressure is high

Correspondence to:
E. Chané,
emmanuel.chane@wis.kuleuven.be

Citation:
Chané, E., J. Saur, R. Keppens, and S. Poedts (2017), How is the Jovian main auroral emission affected by the solar wind?, *J. Geophys. Res. Space Physics*, *122*, 1960–1978, doi:10.1002/2016JA023318.

Received 11 AUG 2016
Accepted 11 JAN 2017
Accepted article online 14 JAN 2017
Published online 23 FEB 2017

Abstract The influence of the solar wind on Jupiter's magnetosphere is studied via three-dimensional global MHD simulations. We especially examine how solar wind density variations affect the main auroral emission. Our simulations show that a density increase in the solar wind has strong effects on the Jovian magnetosphere: the size of the magnetosphere decreases, the field lines are compressed on the dayside and elongated on the nightside (this effect can be seen even deep inside the magnetosphere), and dawn-dusk asymmetries are enhanced. Our results also show that the main oval becomes brighter when the solar wind is denser. But the precise response of the main oval to such a density enhancement in the solar wind depends on the local time: on the nightside the main oval becomes brighter, while on the dayside it first turns slightly darker for a few hours and then also becomes brighter. Once the density increase in the solar wind reaches the magnetosphere, the magnetopause moves inward, and in less than 5 h, a new approximate equilibrium position is obtained. But the magnetosphere as a whole needs much longer to adapt to the new solar wind conditions. For instance, the total electrical current closing in the ionosphere slowly increases during the simulation and it takes about 60 h to reach a new equilibrium. By then the currents have increased by as much as 45%.

1. Introduction

The Jovian main auroral emission is caused not by the interactions between the magnetosphere and the solar wind but by an internal process: namely, the breakdown of corotation (i.e., when, at some radial distance inside the magnetosphere, the magnetosphere-ionosphere coupling cannot accelerate the plasma to rigid corotation anymore). Because of the corotation breakdown, the field lines are bent in the azimuthal direction, which generates a powerful current system, accelerating electrons to high velocities or energies toward the ionosphere [see *Hill*, 2001; *Cowley and Bunce*, 2001]. As a result, it is not trivial to understand whether the solar wind can affect the main oval emission of Jupiter and if it can, how the brightness is affected. The corotation breakdown occurs deep inside the magnetosphere (typically about 30 R_J from the planet, far away from the magnetopause), but variations of the solar wind ram pressure may affect the plasma deep inside the magnetosphere and, as a result, may also affect the main oval.

Observations consistently show that solar wind perturbations and aurorae brightness are positively correlated at Jupiter; see *Barrow* [1978], *Terasawa et al.* [1978], *Barrow* [1979], *Zarka and Genova* [1983], *Barrow et al.* [1986], *Genova et al.* [1987], *Ladreiter and Leblanc* [1989], *Kaiser* [1993], *Baron et al.* [1996], *Gurnett et al.* [2002], *Morioka et al.* [2002], *Prangé et al.* [2004], *Pryor et al.* [2005], *Nichols et al.* [2007], *Clarke et al.* [2009], *Nichols et al.* [2009], *Echer et al.* [2010], *Hess et al.* [2012], *Panchenko et al.* [2013], *Dunn et al.* [2016], and *Badman et al.* [2016]. The majority of these observations were done at radio wavelengths, but infrared observations were performed by *Baron et al.* [1996], ultraviolet observations by *Pryor et al.* [2005]; *Nichols et al.* [2007]; *Clarke et al.* [2009]; *Nichols et al.* [2009]; *Badman et al.* [2016], and X-ray observations by *Dunn et al.* [2016]. For most observations, the spatial resolution was not sufficient to know with certainty to which part of the aurorae the solar wind perturbations were correlated, except for *Nichols et al.* [2007], *Clarke et al.* [2009], *Nichols et al.* [2009], and *Badman et al.* [2016] where it was shown that the main oval brightness increases when the solar wind perturbations reach Jupiter. In most of these studies, the solar wind parameters are not very well constrained: measurement at 1 AU is simply propagated to the orbit of Jupiter, which leads to uncertainties. Nevertheless, it was sometimes possible to use in situ measurements obtained close to Jupiter, e.g., *Barrow et al.* [1986] and

Ladreiter and Leblanc [1989] used Voyager 1 and Voyager 2 measurements and *Gurnett et al.* [2002] and *Nichols et al.* [2007] used data from the Cassini spacecraft.

Even though observations indicate that the main oval brightness and the solar wind ram pressure are positively correlated, it is still not understood why this is the case. We do not know exactly, for instance, how the solar wind influences the azimuthal velocity of the plasma in the magnetosphere, or how the magnetic fields and current systems are affected. In the present paper, we will perform simulations of the interactions between the solar wind and the Jovian magnetosphere in order to understand how variations in the solar wind density (and therefore in the solar wind ram pressure) affect the main oval emission at Jupiter.

2. Physical Setup and Numerical Model

To investigate how the solar wind influences the magnetosphere of Jupiter, we perform three-dimensional one-fluid MHD global simulations using the code MPI-AMRVAC [see *Keppens et al.*, 2012; *Porth et al.*, 2014]. This code is the adaptive mesh refinement version of the VAC code [*Tóth*, 1996]. The equations are solved using the finite volume method with Total-Variation-Diminishing Lax-Friedrichs numerical scheme. The MHD equations are solved in conservative form, and the magnetic field splitting method developed by *Tanaka* [1994] is used. Various problems have already been studied successfully with VAC or MPI-AMRVAC, for instance, the solar wind and coronal mass ejections [*van der Holst et al.*, 2005; *Chané et al.*, 2008], solar prominences [*Keppens et al.*, 2015], relativistic jets [*Monceau-Baroux et al.*, 2015], or even dust dynamics in nebulae [*Hendrix et al.*, 2015].

The physical model which we here use to study Jupiter's magnetosphere has been described in detail by *Chané et al.* [2013]. In a nutshell, our model solves the ideal MHD equations (plus gravity) almost everywhere in the numerical domain, except for two regions where extra source terms are used in the equations. These two regions are (1) the Io torus, where axisymmetric mass loading occurs, adding new plasma in the numerical domain (the mass loading rate is chosen to be 1000 kg/s), and (2) the ionospheric region where the plasma collides with neutral particles, which have a prescribed density and velocity. The collisions transfer momentum from the neutrals to the ionospheric plasma (initiating the rotation of the magnetosphere). In addition, the current systems are closed in this region, and the plasma is heated via Joule heating. The exact equations solved in these two regions can be found in *Chané et al.* [2013].

Our numerical domain extends between 4.5 R_J and 189 R_J in all directions, and spherical coordinates are used. We use three levels of refinement on a static mesh. The smallest cells are 0.25 R_J large, while the intermediate ones are 0.5 R_J large, and the largest ones are 1 R_J large. The smallest cells, which are located in an region of the numerical domain where the radial distance is between 25 R_J and 76.5 R_J and the latitude between −11° and 11°, represent 59% of the total amount of cells, the intermediate cells 17%, and the largest cells 24%. The effective resolution is $800\times128\times128$. This mesh is the same as the one used in the simulation E of *Chané et al.* [2013]. Due to numerical constraints, our ionospheric region is unrealistically large and extends between 4.5 R_J and 8.5 R_J. In addition, the Io torus is located at 10 R_J, instead of 5.9 R_J because we want to have a clear separation between the Io torus and the ionospheric region. Note that in other global simulations of Jupiter's magnetosphere, the inner boundary is located farther away: between 8 R_J in *Moriguchi et al.* [2008] and 30 R_J in *Miyoshi and Kusano* [1997] and that the Io torus is not included.

The drawback of this approach is that our model cannot currently give realistic results within 10 R_J. Nevertheless, since our model is constructed to have the magnetosphere-ionosphere coupling explicitly included in the numerical domain, our results are in good agreement with observations and theory above 10 R_J [see *Chané et al.*, 2013]. In particular, the density profile compares very well with the model, derived from in situ measurements of *Bagenal and Delamere* [2011]; the radial velocity profile is realistic and is similar to the one obtained by *Bagenal and Delamere* [2011]; we are also able to reproduce the plasma velocity dawn-dusk asymmetry measured by *Woch et al.* [2004]; the main oval maps to the region of corotation breakdown as expected by theory [see *Cowley and Bunce*, 2001; *Hill*, 2001]; and the main oval discontinuity in the prenoon sector, first observed by *Radioti et al.* [2008], is also present in our simulations. Finally, our simulations do not produce unrealistic/nonphysical supercorotation that appear in several other models (see, for instance, *Moriguchi et al.* [2008], who presented the first global simulation of the Jovian magnetosphere including an ionosphere but where 200% supercorotation was obtained in some parts of the simulation).

It should be noted that in our simulations, outside of the ionospheric region, the induction equation is simply $\frac{\partial \mathbf{B}}{\partial t} = \nabla \times (\mathbf{v} \times \mathbf{B})$, which implies that in theory, the frozen-in theorem holds and that the plasma should remain

Table 1. Solar Wind Density in Our Simulations

	Simulation 1	Simulation 2	Simulation 3
ρ (amu cm^{-3})	0.162	0.552	1.104

on the same field lines. Nevertheless, numerical diffusion is present in the simulations, and as a result, the frozen-in theorem does not hold. In global simulations of the Jovian magnetosphere, the size of the grid cells is usually such that the numerical resistivity is higher than the physical one. This is why we do not include the resistivity in our equations (i.e., it would almost not affect our results). The radial transport of the logenic plasma is affected by the numerical diffusion, and a very high numerical diffusion would lead to unrealistically high radial velocities in the equatorial plane. Therefore, it is important to check the radial velocity profile in the simulations. This was done in *Chané et al.* [2013], where we compared the radial velocity profiles obtained in our simulations with theoretical predictions (see Figure 5). We showed that the radial velocities were realistic, meaning that the numerical diffusion did not produce an unreasonable plasma transport in our simulations. The same is true for the present simulations, which is not surprising since the equations are solved on the exact same mesh.

To study the influence of the solar wind density on Jupiter's magnetosphere, we performed three simulations. In the first simulation, the solar wind is prescribed as follows: the mass density is $\rho = 0.162$ amu cm^{-3}; the plasma speed is antisunward: with v_x=−400 km/s, v_y=0, and v_z=0; the interplanetary magnetic field is almost in a Parker spiral configuration: $B_x = 0$, $B_y = 0.44$ nT, and $B_z = 0$; the temperature is $T = 15,000$ K, where x is directed toward the Sun, where z points north and coincides with Jupiter's rotation axis, and where y points toward dusk and completes the orthogonal right-handed system. These values are typical for quiet solar wind conditions at the orbit of Jupiter [see *Joy et al.*, 2002]. The second simulation starts with the same solar wind conditions, but once the simulation reaches a quasi steady state (after 328 h), the solar wind density is increased to $\rho = 0.552$ amu cm^{-3}; these conditions are typical for disturbed solar wind conditions [see *Joy et al.*, 2002]. The increase in density is linear and lasts for 1 h. The moment when the high-density region reaches the subsolar bow shock of the Jovian magnetosphere is considered as time $t = 0$. The last simulation is similar to the second one, except that the density increases to $\rho = 1.104$ amu cm^{-3}; this corresponds to very disturbed solar wind conditions. The solar wind density used in our simulations is summarized in Table 1. Note that the solar wind conditions used in simulation 3 are uncommon but that higher solar wind densities have been measured at the orbit of Jupiter. The average value of the solar wind density and the standard deviation has been studied by *Ebert et al.* [2014]. Using two different data sets from the Ulysses spacecraft, they found that the average density is 0.29 amu cm^{-3} (for the first data set) and 0.2 amu cm^{-3} (for the second data set). The corresponding standard deviations were found to be 0.25 amu cm^{-3} and 0.26 amu cm^{-3}. This means that the solar wind density used in simulation 3 is 3.3 to 3.5 standard deviations away from the average value. On the other hand, the solar wind ram pressure in simulation 3 is less uncommon (since we do not increase the solar wind speed). Based on *Ebert et al.* [2014] study, our ram pressure is 2.7 standard deviations away from the average value for data set 1 and 1.3 standard deviations away for data set 2.

In our simulations, we only change the solar wind density, even though, in the interplanetary space, when a perturbation reaches the Jovian magnetosphere, the plasma velocity, the interplanetary magnetic field, and the plasma temperature of the solar wind also change. Our simulations therefore do not fully represent the arrival of a coronal mass ejection or of a corotating interaction region at Jupiter but are rather thought experiments designed to study how the Jovian magnetosphere would be affected if only the solar wind density were to change.

3. How Does the Solar Wind Density Influence the Magnetosphere?

3.1. Magnetic Field

In the present section, we will see how the magnetic field lines of the Jovian magnetosphere are affected by the solar wind, and especially how they are affected by a solar wind density increase. Figure 1 shows selected field lines for simulation 1 (quiet solar wind conditions). The field lines were selected as close as possible to the magnetopause. In the outer magnetosphere (close to the magnetopause) the field lines are bent by the solar wind: bent back in the morning side, and bent forward in the afternoon side. The subsolar magnetopause standoff distance is 73 R_J. On the premidnight sector, long closed field lines reach 170 R_J away from the planet (not visible on the figure). It should be mentioned that the length and shape of the field lines on the nightside vary significantly throughout the simulations (even when the solar wind conditions remain constant). On the

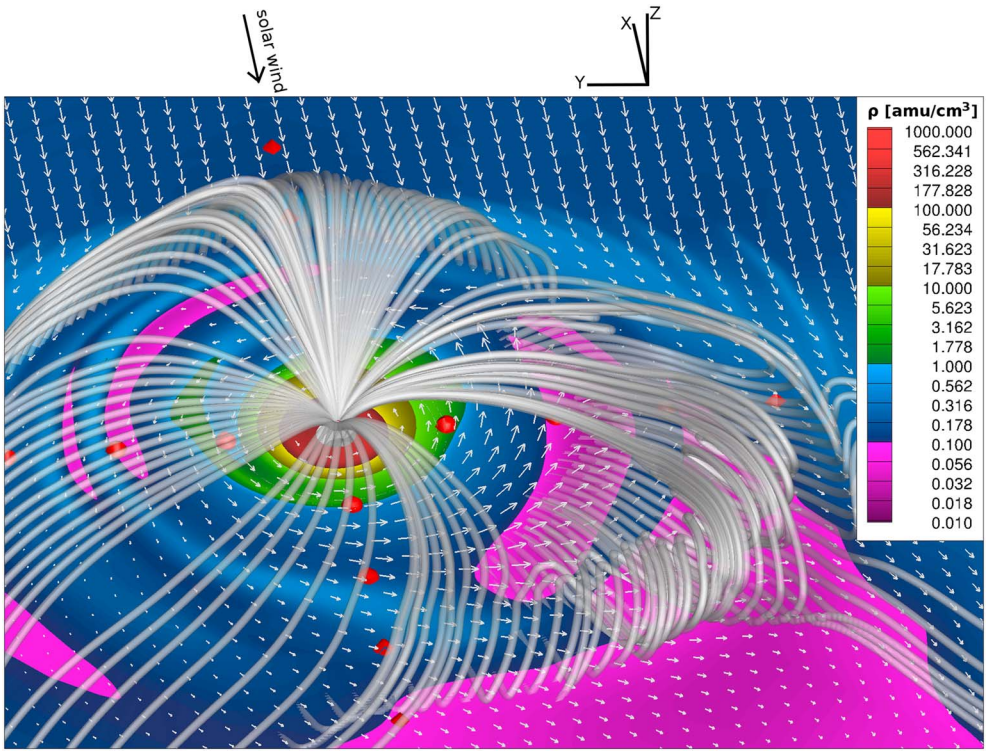

Figure 1. Jupiter's magnetosphere for quiet solar wind conditions (simulation 1) at time t = 9h37m30s. The density in the equatorial plane is shown with color contours. The plasma velocity is represented by white arrows. Selected magnetic field lines are shown in light gray. Red spheres are plotted every 25 R_J along the X axis (between −100 R_J and 100 R_J) and along the Y axis (between −100 R_J and 75 R_J). A plasmoid can be seen in the magnetotail.

postmidnight sector, a large plasmoid is clearly visible. In our simulations, large plasmoids are episodically (but not periodically) ejected in the magnetotail.

The shape of the magnetosphere is affected by the solar wind density. In our simulations, the magnetosphere is, as expected, more compressed (smaller) when the solar wind density (and thus the ram pressure) is high. The release of plasmoids is also affected by the solar wind density: for instance, at t = 9h37m30s, in simulation 3, a plasmoid is also present, but it is located 80 R_J farther away from Jupiter than in simulation 1. This is because the solar wind density affects the time when plasmoids are ejected. *Zieger et al.* [2010] discussed in detail the effect of the solar wind ram pressure on plasmoids' ejection in the case of Saturn. In their simulations plasmoid releases were also affected by the solar wind.

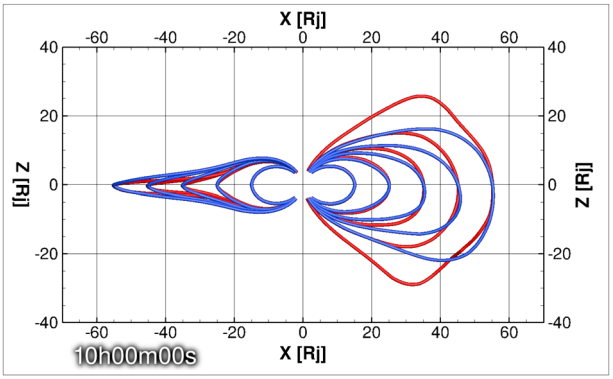

Figure 2. Selected magnetic field lines for simulations 1 (quiet solar wind conditions, in blue) and 3 (very disturbed solar wind conditions in red) 10 h after the high-density solar wind reached the magnetosphere in the noon-midnight meridian (side view). The solar wind comes from the right.

The solar wind density also affects the shape of the magnetic field lines deep inside the magnetosphere. This is illustrated in Figure 2, where selected magnetic field lines are plotted with seeds in the noon-midnight meridian, for simulation 1 and for simulation 3. One can see that when the solar wind ram pressure is higher, the field lines are more compressed on the dayside and more elongated on the nightside, i.e., the day-night asymmetry is more pronounced. Note that global MHD simulations by *Walker et al.* [2001] already showed that when the solar wind ram pressure increases,

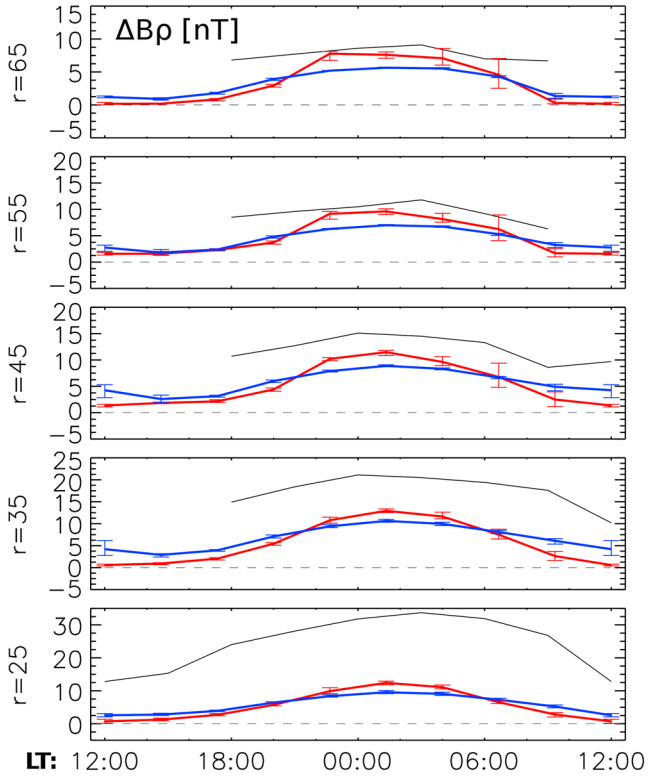

Figure 3. Average values of $\Delta B_\rho = B_\rho - B_\rho^{dip}$ as a function of local time for different radial distance (25, 35, 45, 55, and 65 R_J) for simulations 1 (in blue), and 3 (in red), where B_ρ is the radial component of the magnetic field in cylindrical coordinates and B^{dip} is dipole magnetic field of Jupiter. The values are averaged over time and over latitude (between −10° and 10°). The vertical bars represent the minimal and maximal values that occurred during the whole simulation. The black lines show the values measured by the Galileo spacecraft in the lobes, taken from *Khurana* [2001].

the magnetic field lines on the dayside become more dipole-like. The day-night asymmetry in our simulation is not surprising for field lines close to the magnetopause, but the field lines are also affected deep inside the magnetosphere. This means that the solar wind can affect the magnetosphere, even very far from the magnetopause. This is consistent with asymmetries measured deep in the Jovian magnetosphere: in the magnetic field [*Khurana*, 2001] and in the plasma flow (*Woch et al.* [2004] showed that the plasma rotates slower at dusk than at dawn).

Figure 3 shows the radial component of the magnetic field, where the internal component arising in our model from a dipole field only has been subtracted, as a function of local time for different radial distances for simulations 1 and 3. A comparison with measurements obtained by the Galileo spacecraft from *Khurana* [2001] is also provided in this figure. We see that in both simulations, as well as in the in situ measurements, the radial component of the magnetic field is stronger on the nightside (even deep inside the magnetosphere). This is in agreement with Figure 2: field lines are compressed by the solar wind on the dayside and elongated on the nightside. For low radial distances, the asymmetry is stronger in the measurements than in the simulations (by a factor of 2 or 3). This is probably because the current sheet magnetic field is not taken into account by *Khurana* [2001] (only the lobes), whereas the whole region between −10° and 10° latitude is considered in our simulations. The figure shows that the higher the solar wind density is, the stronger this day-night asymmetry is. For simulation 3 (very disturbed solar wind conditions), ΔB_ρ is sometimes negative on the dayside. This means that the compression caused by the solar wind is stronger than the effects of the radial transport of the magnetic field and that as a result, the magnetic field lines are sometimes more compressed than dipole field lines. This is typically what is expected in the cushion region [a region adjacent to the dayside magnetopause where the magnetic field is quasi-dipolar and where the plasma density is low; see *Went et al.* 2011, and references therein].

The azimuthal magnetic field is shown in Figure 4, for simulations 1 and 3, as well as the measurements obtained by the Galileo spacecraft from *Khurana* [2001]. A clear dawn-dusk asymmetry can be seen in the simulations and in the measurements. It shows that the field lines are more bent back at dawn than at dusk. Again, the higher the solar wind density is, the stronger this asymmetry is. This is interesting because, as we will see in detail in section 5, the bent back field lines generate the radial currents responsible for the main auroral emission. The vertical bars of Figures 3 and 4 show us by how much the plotted quantities vary during the simulations. It is interesting to see that there are more variations in the postmidnight sector. This is where the Vasyliunas X line is located. These variations are caused by plasmoids being ejected, the field lines are then greatly affected and change drastically.

Figure 5 (top) displays B_z as a function of local time in the equatorial plane at 30 R_J at time t = 90 h for simulations 1 and 3. One can see a strong day-night asymmetry with B_z being more negative at noon than

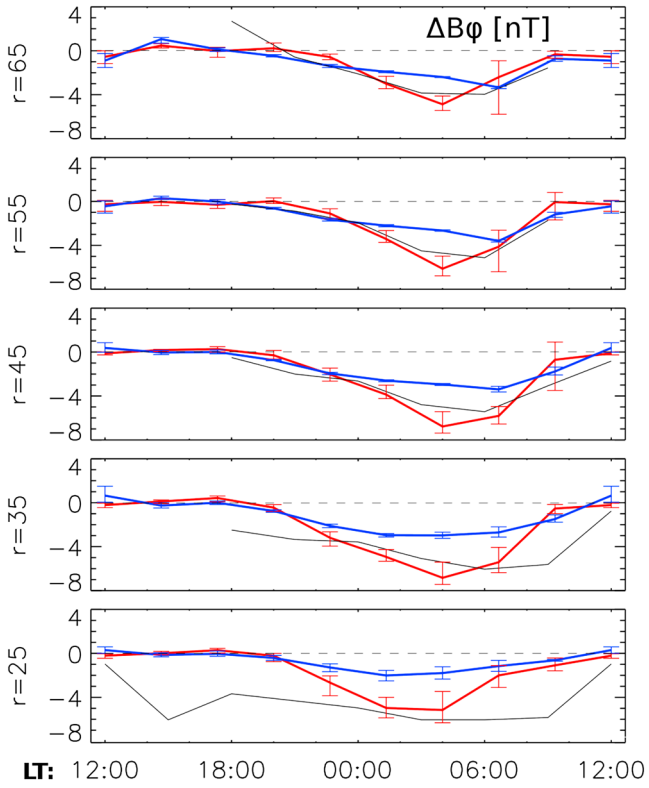

Figure 4. Same as Figure 3 but for B_ϕ instead of ΔB_ρ.

at midnight. This is because the solar wind compresses the field lines on the dayside (which increases the strength of the magnetic field), while the field lines get elongated on the nightside (decreased magnetic field strength). The asymmetry is large: B_z is 3 times more negative on the dayside than on the nightside for simulation 1 and 7 times more negative for simulation 3.

Figure 5 (middle) shows B_ϕ, in a plane 5 R_J north of the equatorial plane as a function of local time. One can see that there is almost no bent back on the dayside and at dusk, while a strong bent back is seen on the nightside and at dawn. This asymmetry is stronger for simulation 3 (very disturbed solar wind conditions).

3.2. Plasma Circulation

We have seen that the magnetic field in the Jovian magnetosphere displays asymmetries (e.g., day-night asymmetries and dawn-dusk asymmetries) even deep inside the magnetosphere. In the present section, we will show that the plasma circulation is also strongly affected by variations in the solar wind and also displays strong asymmetries. Figure 6 shows the azimuthal plasma velocity as well as the velocity vectors in the equatorial plane for simulations 1 and 3 at $t = 90$ h. This figure clearly shows that the plasma rotates faster at dawn than at dusk in our simulations. This asymmetry is well known and has been observed by the Galileo spacecraft [see *Woch et al.*, 2004; *Krupp et al.*, 2004]. In our simulations, this asymmetry is stronger when the solar wind density is higher. Again, this is not a surprise: any local time asymmetry is by essence coming from the solar wind, so increasing the solar wind ram pressure enhances this asymmetry.

Dawn-dusk asymmetries for the azimuthal velocity were also obtained by *Fukazawa et al.* [2006] in their global simulations of the Jovian magnetosphere. In their simulations, the solar wind ram pressure also affects this asymmetry. But their simulation results display some differences with ours: (1) they observe that at dawn the corotation extends up to 120 R_J, (2) they obtain inward flows around 15:00 LT (especially when the solar wind ram pressure is high) which seem to produce lower speeds on the afternoon side, and (3) when the solar wind ram pressure is low, they obtain negative azimuthal velocities (anticorotation) in the cushion region. Even though their results are different from ours, there are some similarities: (1) enhanced dawn-dusk asymmetries when the solar wind ram pressure is high and (2) low azimuthal velocities in the postnoon sector.

Note that temporal variations are present in our simulations and that Figure 6, although it is mostly representative of typical azimuthal velocities in our simulations, is only a snapshot at $t = 90$ h. It therefore displays some transient features. For instance, the extremely low azimuthal velocity in the postnoon sector around 40 R_J for simulation 3 is not always present. Ten hours before, at $t = 80$ h, the azimuthal velocities in this region were higher (namely, between 34 and 220 km/s).

The departure from corotation occurs farther away at dawn compared to dusk. Note that this does not necessarily mean that the maximum parallel currents (responsible for the main oval) occur at larger radial distances at dawn than at dusk or that the main oval latitude would be higher at dawn than at dusk. The position of the maximum value in field-aligned currents in the equatorial plane is influenced by the shape of the azimuthal velocity profile at a given local time, as well as by the shape of the magnetic field lines. In addition, one should also keep in mind that a maximum in the $\mathbf{j} \times \mathbf{B}$ force does not mean a maximum in azimuthal velocity but a

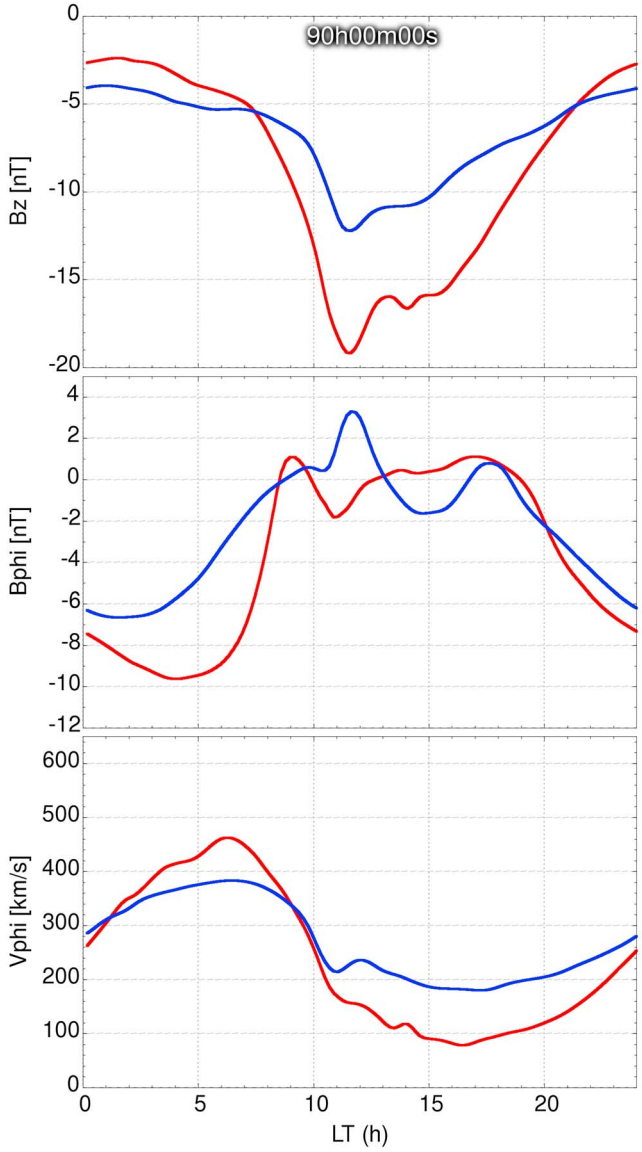

Figure 5. *Z* component of the magnetic field in the (top) equatorial plane at a radial distance of 30 R_J as a function of local time, (middle) azimuthal magnetic field at a radial distance of 30 R_J, in a plane 5 R_J north of the equatorial plane as a function of local time, and (bottom) azimuthal plasma velocity in the equatorial plane at a radial distance of 30 R_J as a function of local time at $t = 90$ h for simulations 1 (in blue) and 3 (in red).

maximum acceleration if no other forces balance $\mathbf{j} \times \mathbf{B}$ at this location. Thus, the maximum azimuthal velocity tends to be phase delayed with respect to the maximum $\mathbf{j} \times \mathbf{B}$ (typically by 60° in our simulations).

The magnetopause is closer to Jupiter for simulation 3. Once the high-density solar wind reaches the magnetosphere, the inward motion of the magnetopause happens in a few hours only. In 5 h, the subsolar magnetopause moved 16 R_J inward for simulation 3 and 12 R_J inward for simulation 2. Note that the position of the magnetopause keeps slightly changing throughout the simulations, even when the solar wind is constant. This is for instance caused: by reconnection with the interplanetary magnetic field on the dayside, by constantly changing mass repartition inside the magnetosphere when the magnetosphere rotates, or by plasmoid release in the magnetotail. The position of the magnetopause as a function of the solar wind ram pressure was already studied via global MHD simulations by *Walker et al.* [2001], but their results cannot directly be compared with our results since different solar wind ram pressures were used.

The azimuthal velocity at 30 R_J in the equatorial plane for simulations 1 and 3 is displayed in Figure 5 (bottom). We see that the azimuthal velocity is 5.8 times higher at dawn than at dusk for simulation 3 and twice higher

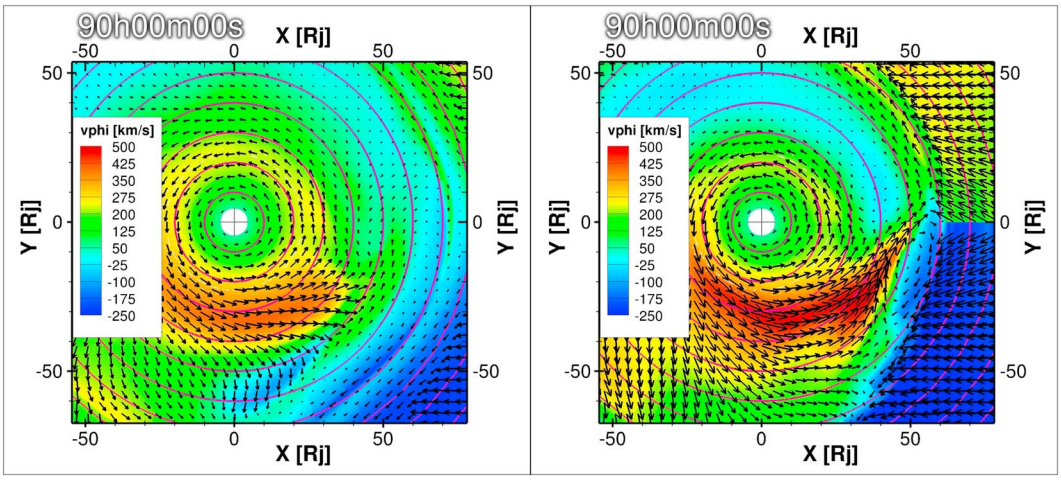

Figure 6. Azimuthal plasma velocity (color coded) and velocity vectors in the equatorial plane for (left) simulation 1 and (right) simulation 3 at time $t = 90$ h. Concentric circles are drawn every 10 R_J. The solar wind comes from the right.

for simulation 1. A sharp transition is also present in the prenoon sector for both simulations (discussed in detail in section 6).

It should also be mentioned that the plasma density and the plasma pressure in the magnetosphere are affected by the solar wind conditions: they tend to increase when the magnetosphere is compressed. In our simulations, the density and the pressure in the plasma sheet display strong temporal variations. This is mostly due to high-density regions (mainly forming a spiral pattern, see Figure 1) rotating around Jupiter. We therefore did not include a panel showing the density in Figure 5: a snapshot at a given time would not adequately be representative of the situation. Nevertheless, one can average the values for a sufficient time length and compare the results in different simulations. For example, during the 20 last hours of the simulations, in the equatorial plane, at 40 R_J, averaged over all local times, the density in simulation 3 is 80% higher than in simulation 1, while the plasma pressure is 2.1 times higher. Closer to the planet, at 30 R_J, the increases in density and pressure are more moderate: 28% and 38%, respectively.

4. How Does the Solar Wind Density Influence the Ionospheric Currents?

We will now investigate how the ionospheric currents are affected by the solar wind density. In our simulations, the electrical currents cannot cross the inner boundary. They close in the ionospheric region via Pedersen and Hall currents. Furthermore, as shown in *Chané et al.* [2013], the magnetic field lines emanating from the main oval in our simulations map to the position of the corotation breakdown in the equatorial plane. Our simulations are thus in agreement with theoretical predictions [see *Cowley and Bunce*, 2001; *Hill*, 2001]. Figure 7 displays the temporal evolution of $j_{\parallel}/B$ mapped into the ionosphere of Jupiter physically located at 1 R_J (which is a proxy for the aurora brightness and was estimated to be about 10^{-4} A m^{-2} T^{-1} in the main oval by *Clarke et al.* [2004]) for simulations 1 (top row) and 3 (middle row). It also shows the differences between simulations 3 and 1 (bottom row). The auroral electrons which excite the emission within Jupiter's atmosphere are accelerated several radii above Jupiter's atmosphere. The exact location of the acceleration region along the field lines is unknown and will be measured by the spacecraft JUNO. The auroral electrons are accelerated on field lines with large electric currents and move along the same field lines into Jupiter's atmosphere (e.g., *Hill*, 2001; *Cowley and Bunce* [2001] and for the Earth [*Knight*, 1973]). Therefore, Figure 7 displays the expected locations of the auroral ovals based on the magnetospheric current system driven in our model. For both simulations, the main oval is located around 15° colatitude and is brighter on the nightside than on the dayside. Note that *Walker and Ogino* [2003], in their global MHD simulations, also obtained stronger ionospheric currents on the nightside than on the dayside. In our simulations, the main oval is also slightly brighter at dusk than at dawn. This dusk-dawn asymmetry of the brightness of the main oval has been observed by *Bonfond et al.* [2015].

Figure 7, in particular the bottom row, illustrates how the main auroral emission becomes brighter when the solar wind density increases. This enhancement is slightly more pronounced at dusk than at dawn and on

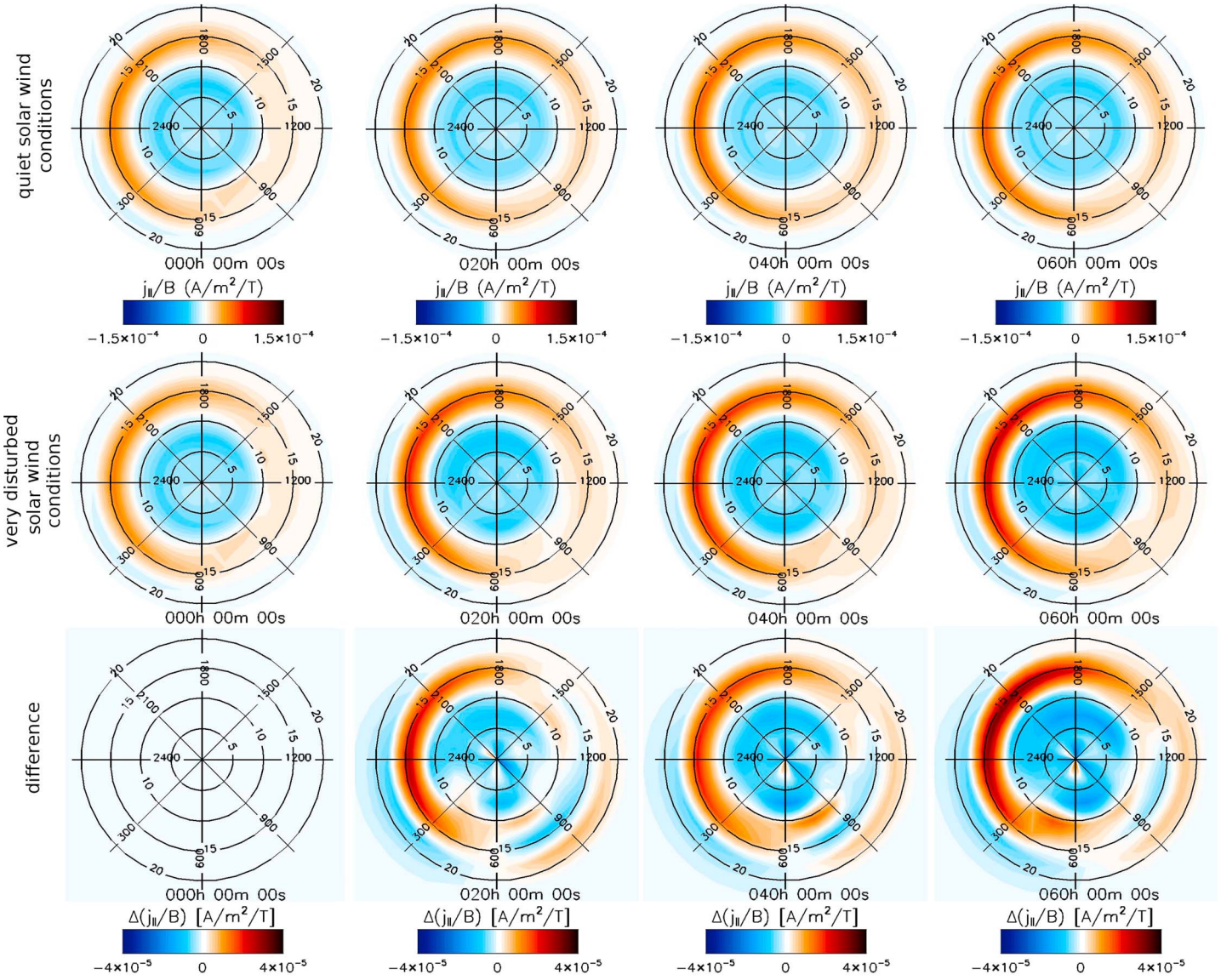

Figure 7. $j_{\parallel}/B$ in the ionosphere (northern hemisphere) for (top row) simulation 1 and (middle row) simulation 3 as well as (bottom row) the difference between simulations 3 and 1 for (first column) $t=0$ h, (second column) $t=20$ h, (third column) $t=40$ h, and (fourth column) $t=60$ h. Local time and colatitude are overplotted in black. The Sun is located on the right.

the nightside than on the dayside. Our simulations are in agreement with observations: an enhancement of the solar wind ram pressure leads to an enhancement of the brightness of the main oval. *Nichols et al.* [2007], for instance, showed that the main oval was 2 to 3 times brighter during compression periods than during rarefaction periods. Figure 7 also shows that in our simulations, the location of the main oval changes by a few degrees on the prenoon sector. In addition, the main oval discontinuity, a darker region in the prenoon sector of the main oval observed by *Radioti et al.* [2008], becomes more pronounced for simulation 3 (very disturbed solar wind conditions).

In addition, on the dayside, the main oval is broader for simulation 3 than for simulation 1. In our simulations, the main oval needs approximately 60 h to adapt to the new solar wind conditions and to reach a new quasi steady state. It should also be noted that in our simulations, it takes 2h35m to see any changes in the ionospheric currents once the high-density solar wind has reached the magnetosphere: the main oval currents and the return currents in the postnoon sector first slightly decrease.

Figure 8 shows the peak value of $\frac{j_{\parallel}}{B}$ as a function of local time, for simulations 1, 2, and 3, at t = 107h15m. We see that the values are similar on the dayside for the three simulations, meaning that the solar wind density

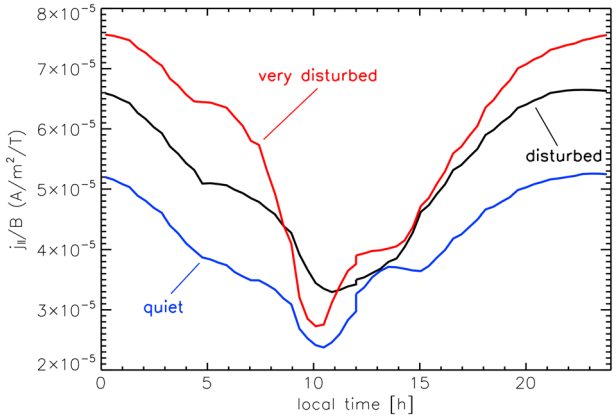

Figure 8. Peak value of $\frac{j_{\parallel}}{B}$ in the ionosphere after 107h15m as a function of local time for simulations 1 (in blue), 2 (in black), and 3 (in red).

almost does not affect the peak value of $\frac{j_{\parallel}}{B}$ on the dayside. On the other hand, the peak value of $\frac{j_{\parallel}}{B}$ on the nightside is clearly different for the three simulations. The higher the solar wind density is, the higher this value is. At 00:00 LT, the peak value of $\frac{j_{\parallel}}{B}$ is 27% higher for simulation 2 than for simulation 1, and 45% higher for simulation 3 than for simulation 1. But since the main oval on the dayside is broader for simulation 3 (see Figure 7), even if the peak value of $\frac{j_{\parallel}}{B}$ is similar for the three simulations at noon local time, the total field-aligned currents flowing to the main oval are not. This can be seen on Figure 9 where we integrate $\frac{j_{\parallel}}{B}$ over all latitudes of the main oval and plot it as a function of local time. One can see that for all local times, the higher the solar wind density is, the stronger the currents are. The total increase in the parallel currents in the main oval between simulations 1 and 3 is 37% on the dayside and 49% on the nightside.

Figure 10 shows how the total electrical current closing in the ionosphere increases with time for simulations 1, 2, and 3. First of all, we see that it takes several rotation periods (more than 60 h) for the ionosphere to adjust to the new solar wind conditions. Once the simulations reached a new quasi steady state, the total ionospheric current is 32% higher in simulation 2 than in simulation 1 and 45% higher in simulation 3 than in simulation 1. As long as the solar wind density remains high, the ionospheric current remains high, meaning that this increase is not a transient phenomenon but is caused by the new steady state equilibrium of the magnetosphere. Second, time variations independent of the solar wind conditions are clearly visible in Figure 10. The variations include the 9h55m rotational periodicity of Jupiter superposed with the magnetospheric adjustments due to intrinsic dynamical properties of Jupiter's magnetosphere, such as plasmoid releases. For instance, the deep long through present around $t = 75$ h for simulation 3 is related to the ejection of a huge plasmoid in the tail. Although several smaller plasmoids were released during the simulations, this plasmoid was the only one having a clear influence on the amount of electrical current closing in the ionosphere.

Our simulations indicate that the strength of the ionospheric electrical current is affected much more by the strength of the solar wind ram pressure, with the duration of the event playing an important role, than by the variations of this strength. In other words, we face a quasi steady state problem with new boundary conditions (i.e., the position of the magnetopause), rather than a time-dependent problem, where, for instance, the motion of the magnetopause would play the dominant role. At the beginning of the simulations, when the solar wind ram pressure increases, at first the currents did not change much, but they slowly increased for several rotation periods before reaching their maximum. This is because the magnetosphere as a whole was slowly changing due to the new solar wind conditions: the position of the magnetopause changed, the shape of the magnetic field lines also changed, and the amount of plasma in the magnetosphere as well. Conversely at the beginning of the simulations,

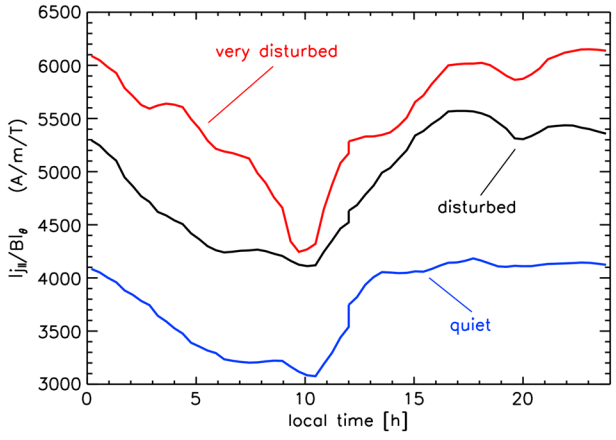

Figure 9. $\frac{j_{\parallel}}{B}$ in the ionosphere integrated over all latitudes of the main oval after 107h15m as a function of local time for simulations 1 (in blue), 2 (in black), and 3 (in red).

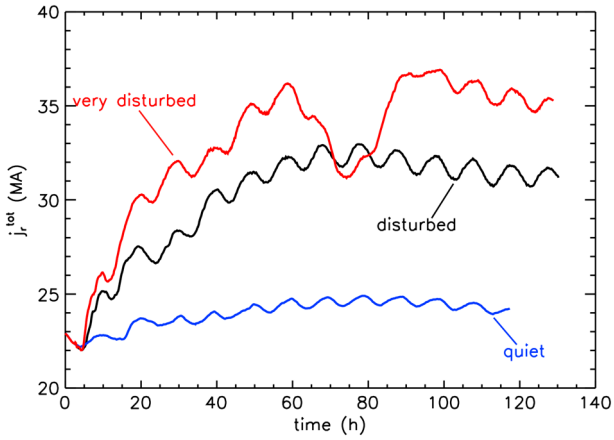

Figure 10. Total electrical current closing in the ionosphere as a function of time for simulations 1 (in blue), 2 (in black), and 3 (in red). The currents were integrated through a sphere of radius 6.8 R_J centered at Jupiter. Note: the trough located around 75 h for simulation 3 is caused by the ejection of a huge plasmoid in the tail.

when the magnetopause rapidly moved inward, the total ionospheric currents shown in Figure 10 almost did not change.

Figure 11 shows the peak value of $\frac{j_{\parallel}}{B}$ in the ionosphere in the main oval at 12:00 LT for the three simulations, for the first hours after the high-density solar wind reached the magnetosphere. For the first 160 min, the values are the same in all simulations, then the strength of the ionospheric field-aligned currents decreases for simulations 2 and 3, and the decrease is the strongest for very disturbed solar wind conditions: the decrease was 15% for simulation 2 (disturbed solar wind condition) and 19% for simulation 3 (very disturbed solar wind conditions). But this decrease in the intensity of the peak value of the field-aligned current does not last long. After 260 min, the current is already stronger for simulation 3. So at the beginning of the simulation, on the dayside, the ionospheric currents and the solar wind ram pressure are anticorrelated, whereas later in the simulations, they are correlated.

It should be noted that what we observe in Figure 11 is in agreement with theories [*Cowley and Bunce*, 2001; *Southwood and Kivelson*, 2001; *Cowley and Bunce*, 2003], which predict that when the solar wind ram pressure increases, the magnetopause and the magnetospheric plasma are pushed inward. Then, because the angular momentum is conserved, the plasma rotating around the planet gets accelerated, decreasing the stress on the field lines and the available currents in the corotation enforcing current system responsible for the main auroral emission. As a result, the brightness of the main emission decreases. This is what we see in our simulations, at least on the dayside and at the very beginning of the simulations. We do not see this phenomenon on the nightside, because the plasma is not pushed inward by the denser solar wind on that side of the planet. And this brightness decrease is only observed at the beginning of the simulation because the plasma is only pushed inward once: when the high-density solar wind reaches the magnetosphere: this is a transient phenomenon (with a typical duration of 100 to 150 min in our simulations).

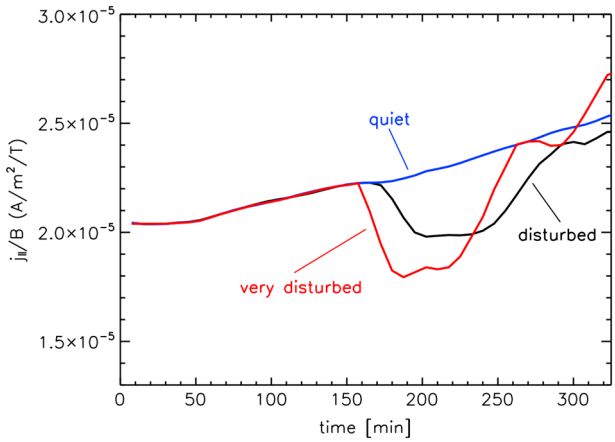

Figure 11. Peak value of $\frac{j_{\parallel}}{B}$ in the ionosphere at 12:00 LT as a function of time for simulations 1 (in blue), 2 (in black), and 3 (in red).

5. Currents in the Equatorial Plane

In the present section, we will investigate how the electrical currents in the equatorial plane are affected by changes in the solar wind density. This will help us to understand why the ionospheric field-aligned currents become stronger when the solar wind density increases.

Figure 12 shows the current density (strength and direction) in the equatorial plane for simulations 1 and 3. We can see that for both simulations, the current is mostly azimuthal (ring current) and that it is maximum around 02:00 LT at approximately 30 R_J from the planet. Note that this is the local time where the field lines

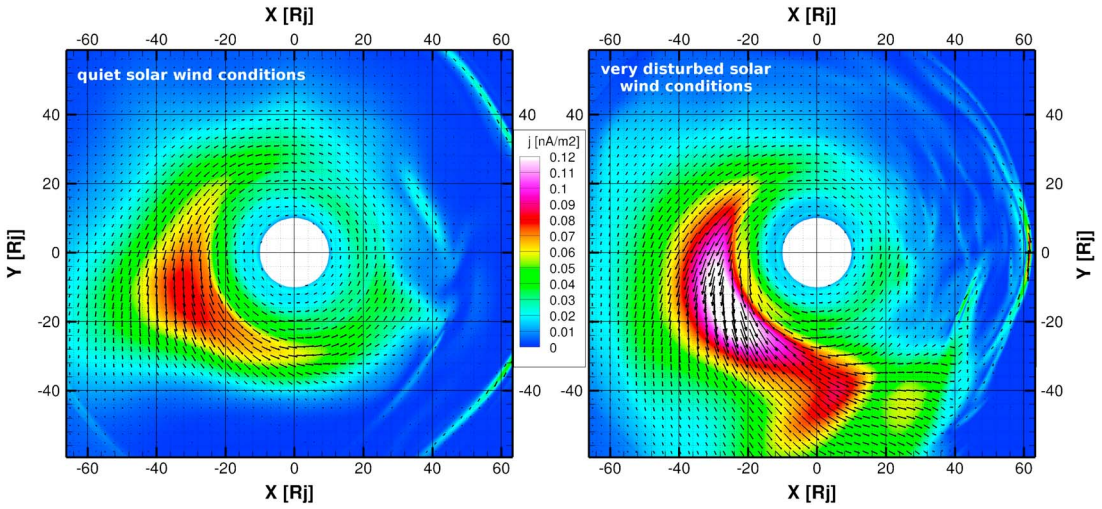

Figure 12. Current density in the equatorial plane (left) for simulation 1 and (right) for simulation 3 at $t = 90$ h. The color contours display the magnitude and the arrows the direction. The Sun is on the right. Note that the numerical domain is larger than what is plotted here and extends up to $r = 189R_J$.

are the most elongated (see Figure 3). In the equatorial plane, the Lorentz force associated with the azimuthal current acts to prevent the plasma to move radially away, i.e., it approximately balances the centrifugal force and the pressure gradient forces. The azimuthal current is indeed associated with the magnetic tension of the elongated magnetic field lines. It is therefore expected to find the maximum current density where the field lines are the most elongated.

Figure 12 also shows that these strong electrical currents in the equatorial plane are weaker for simulation 1 than for simulation 3. The solar wind is causing the day-night and the dawn-dusk asymmetry in the magnetosphere. Therefore, the stronger the solar wind becomes, the more pronounced these asymmetries are, which explains why larger currents are driven in simulation 3.

Although Figure 12 is very useful to understand where the electrical current is maximum in our simulations, it does not show how much of this current is closed in the ionosphere via field-aligned currents (thus producing aurorae). Because j_θ is zero in the equatorial plane, pointing north above the plane and south below it (or vice versa), we instead plot $-\frac{\partial(\sin\theta\, j_\theta)}{\partial\theta}$, which is positive when the electrical current flows inside the equatorial plane and negative otherwise (see Figure 13a). One can clearly see the equatorial contribution to the main oval on this image (especially in the postmidnight sector); unfortunately, it does not let us know whether the radial or the azimuthal currents are responsible for the field-aligned currents. But since $\nabla \cdot \mathbf{j} = 0$, we have

$$-\frac{\partial\left(\sin\theta\, j_\theta\right)}{\partial\theta} = \frac{\sin\theta}{r}\frac{\partial\left(r^2 j_r\right)}{\partial r} + \frac{\partial j_\phi}{\partial\phi}, \tag{1}$$

where the first term on the right-hand side is the contribution of the radial currents (shown on Figure 13b) and the second term is the contribution of the ring current (Figure 13c). One can see that in our simulation, the radial current contribution is, by far, more important than the azimuthal current contribution. We will now see what generates the radial equatorial currents responsible for the main auroral emission in our simulations.

Since

$$j_r = \frac{1}{\mu_0 r\sin\theta}\left(\frac{\partial\left(\sin\theta\, B_\phi\right)}{\partial\theta} - \frac{\partial B_\theta}{\partial\phi}\right), \tag{2}$$

equation (1) can be rewritten as

$$-\frac{\partial\left(\sin\theta\, j_\theta\right)}{\partial\theta} = \frac{\partial j_\phi}{\partial\phi} + \frac{1}{r\mu_0}\frac{\partial}{\partial r}\left(r\frac{\partial\left(\sin\theta\, B_\phi\right)}{\partial\theta}\right) - \frac{1}{r\mu_0}\frac{\partial}{\partial r}\left(r\frac{\partial B_\theta}{\partial\phi}\right). \tag{3}$$

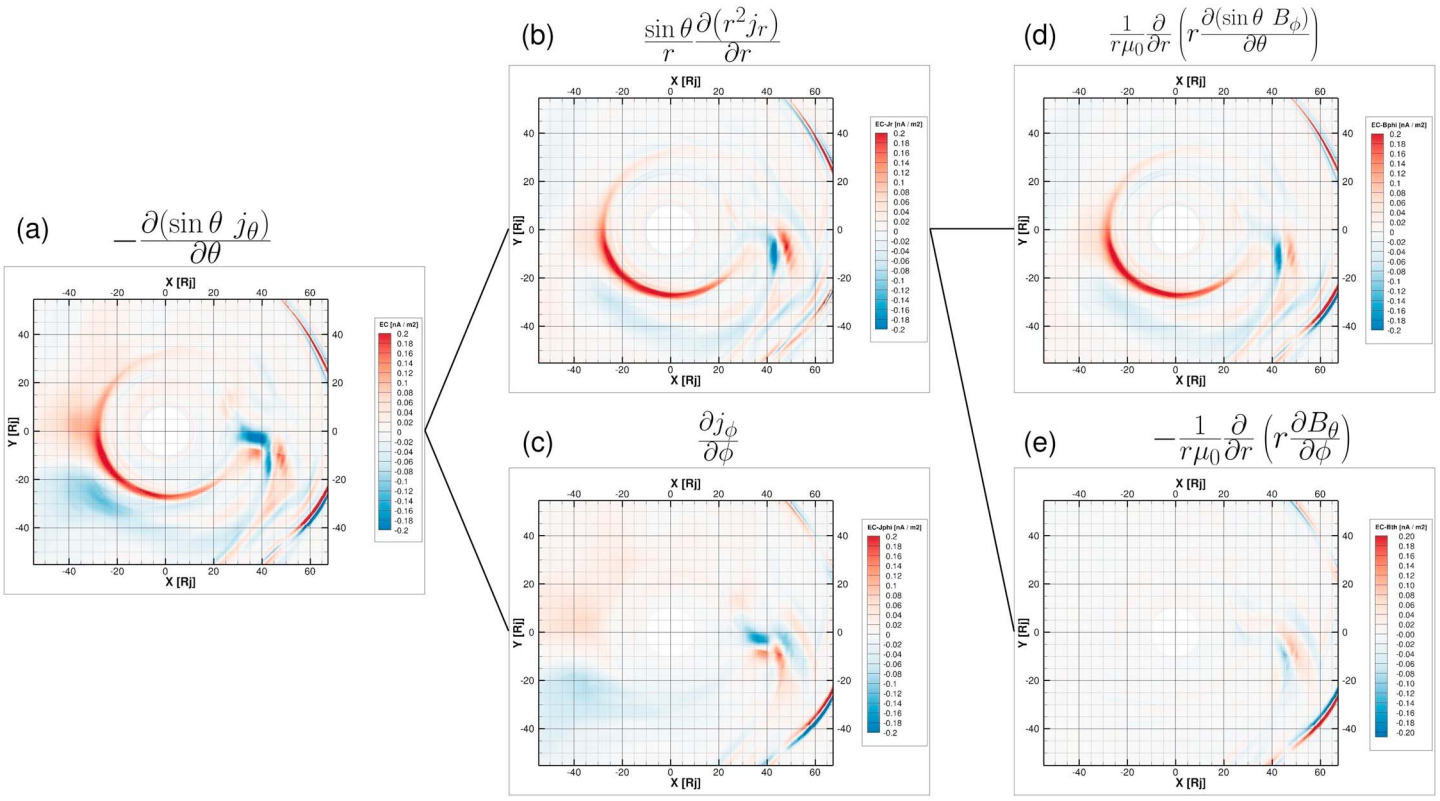

Figure 13. (a) $-\frac{\partial(\sin\theta\, j_\theta)}{\partial\theta}$ in the equatorial plane at time $t = 65$ h for simulation 1. The currents pointing toward the equatorial plane (responsible for the aurorae in the ionosphere) are displayed in red, while the currents pointing out of the plane (that do not generate aurorae in the ionosphere) are displayed in blue. (b) The contribution of the radial electrical current and (c) the contribution of the azimuthal current. (d) The contribution of the radial currents generated by the bent back of the magnetic field lines and (e) the contribution of the radial currents generated by the local time asymmetry of B_θ. The Sun is located on the right.

We see that two phenomena contribute to the closure of radial currents via field-aligned currents: (1) the second term of the right-hand side, which represents the contribution of the bent back of the magnetic field lines (plotted in Figure 13d); and (2) the last term of the right-hand side of the equation, which represents the contribution arising from local time asymmetries in the magnetic field strength and how they change with radial distance (see Figure 13e). One can clearly see in Figure 13 that the main contributor to the main oval is the radial current associated with the bent back of the magnetic field lines. In other words, in our simulations the main contributor to the ionospheric currents is the corotation enforcing current system theorized by *Cowley and Bunce* [2001] and by *Hill* [2001].

6. What Generates the Local Time Asymmetries?

There are two kind of asymmetries in our simulations as well as in the in situ measurements: (1) the day-night asymmetries (e.g., radial component of the magnetic field, strength of the magnetic field, and brightness of the main oval) and (2) the dawn-dusk asymmetries (e.g., plasma azimuthal velocity, bent back of the field lines, and to a lesser degree, brightness of the main oval). All these asymmetries come from the solar wind.

Due to solar wind ram pressure, on the dayside, the magnetic field lines are more dipolar, more compressed (see Figure 2). The shape of these field lines makes it more difficult for subcorotating plasma to produce strong azimuthal magnetic field. On the other hand, on the nightside, where the field lines are very elongated, subcorotating plasma easily produces strong azimuthal magnetic field. Since the magnetic tension associated with the bent back of the field lines accelerates the plasma in the azimuthal direction, this explains why in Figure 5 the azimuthal velocity increases on the nightside and decreases on the dayside.

The azimuthal velocity of the plasma is mainly affected by two phenomena (1) the radial transport, which acts to decrease the azimuthal plasma velocity, due to the conservation of angular momentum, and (2) the Lorentz

force associated with the bent back of the field lines, which increases the azimuthal velocity of the plasma. Note that a bent forward configuration decreases the azimuthal velocity of the plasma, but this occurs rarely. In addition, these two effects are coupled: the azimuthal plasma velocity influences the shape of the field lines. In particular, strong subcorotation generates bent back. Pressure gradients in the azimuthal direction can also affect the azimuthal velocity (as we have shown in *Chané et al.* [2013]), but they will be neglected in the present discussion, as a first approximation.

For the sake of argument, let us follow an imaginary field line around Jupiter. We start at a position where the solar wind cannot force the field line in a compressed dipolar shape. This begins to happen on the postnoon sector, where the radial motion of the field lines is not hindered by the presence of the magnetopause any more, somewhere around 17:00 LT. From this location, because of the radial transport of plasma, this field line will become more and more elongated while traveling around Jupiter. This, combined with the fact that the plasma is subcorotating, will increase the bent back of the field line. This can clearly be seen in our simulation (Figure 5) where B_ϕ becomes more negative between the postnoon sector and the postmidnight sector (the exact local time depends on the simulation).

Since the bent back increases, the Lorentz force, which acts to accelerate the plasma back to corotation, increases as well. In other words, the magnetic tension in the azimuthal direction increases with increasing local time. This explains why the azimuthal velocity of the plasma on our imaginary field line also increases between the postnoon and the postmidnight sector (see Figure 5).

On the post midnight sector, because of the radial transport of plasma, the field line continues to become more and more elongated. This should normally increase the bent back, but since the plasma on this field line rotates faster and faster around Jupiter, the bent back actually starts to decrease. This occurs at 02:00 LT for simulation 1 and at 04:00 LT for simulation 3. In this sector, the plasma on the field line still experiences a strong acceleration in the azimuthal direction due to the strong bent back of the field line. But approximately at dawn, the bent back is now too weak and the azimuthal velocity of the plasma starts to decrease. This is also approximately when the field lines start to be compressed by the solar wind again. This compression dramatically reduces the bent back. The Lorentz force is now much weaker and the azimuthal velocity drops rapidly. The field line and the frozen-in plasma finally finish their orbit around Jupiter, marking the end of our thought experiment. Thus, the dawn-dusk asymmetry is an effect of the solar wind stresses on the magnetosphere combined with rotationally dominated convection patterns within the magnetosphere.

7. Discussions

7.1. On the Importance of Global MHD Simulations

Global MHD simulations are an important tool to study Jupiter's magnetosphere and have several advantages: they are fully three-dimensional in space and are time explicit and thus include radial, azimuthal, and latitudinal asymmetries and their temporal evolutions. Whereas analytical models of the magnetosphere-ionosphere coupling at Jupiter usually need to assume certain symmetries to analytically treat the problem. Although analytic models have limitations, they have tremendously advanced our understanding of the key physical mechanism at work within Jupiter's magnetosphere. We therefore present here a short overview of these models and explain the major differences between them and global MHD simulations.

Hill [1979, 2001] computed the plasma angular velocity in the Jovian magnetosphere and showed that it was affected by the plasma outflow rate and by the ionospheric conductance. In this model, the following simplifying assumptions were made: (1) the magnetic field in the Jovian magnetosphere is a dipole and (2) the plasma outflow rate is constant in the magnetosphere. *Cowley and Bunce* [2001] studied the effect of the assumed magnetic field on the magnetosphere-ionosphere coupling. They used a more realistic empirical model for the magnetic field but, instead of calculating the plasma angular velocity, like *Hill* [1979], they also used an empirical plasma angular velocity. *Pontius* [1997] and *Cowley et al.* [2002] both used a nondipolar empirical magnetic field and computed the equatorial plasma angular velocity using *Hill* [1979] theory. *Pontius and Hill* [1982] studied how the local ionization of neutral gas affects the plasma azimuthal velocity. *Saur et al.* [2004] model include both the plasma outflow rate and the local ionization to calculate the azimuthal velocity. Their model was developed for Saturn but can easily be adapted to Jupiter's magnetosphere and was used to benchmark

Chané et al. [2013] model. A detailed comparison between the two models is presented in *Chané et al.* [2013]. It showed quantitative agreement between theoretical plasma angular velocity and simulation results. Note that to account for local time asymmetries and temporal variation, which are present in our simulations but not in Hill's theory, our results were averaged over all local times and over a Jovian rotation period.

Nichols and Cowley [2004] included the enhancement of the ionospheric conductance caused by electron precipitation, which is important in regions of strong upward field-aligned currents, in the *Cowley et al.* [2002] model. Note that although this process is not included in our simulations yet, it would be possible to implement it in the future. *Nichols and Cowley* [2005] and *Hill* [2009, 2010] showed that the linear approximation of the Knight current-voltage relationship [*Knight*, 1973] cannot be used at Jupiter and that the field-aligned potentials affect the ionospheric field-aligned currents. This is also not implemented in our simulations yet and will be taken into account in subsequent studies.

In calculations made by *Tao et al.* [2010] the influence of the solar radiation on the ionospheric conductance was taken into account: using an empirical magnetic field model, they calculated the plasma angular velocity and the field-aligned currents. Again, this is not implemented in our simulations yet, but making the ion-neutral frequency a function of the local time in our model is straightforward and will be done in future studies.

Nichols [2011] did not use an empirical magnetic field model but instead calculated the magnetic field based on the *Caudal* [1986] model. *Nichols et al.* [2015] then included the plasma pressure anisotropy in their model. Note that even though the plasma pressure anisotropy is not included in our model yet, global MHD simulations taking into account the anisotropy do exist (see, for instance, *Meng et al.* [2012] who simulated the interactions between the solar wind and the Earth's magnetosphere and included the plasma pressure anisotropy in their model).

Although some of these models use physics not included yet in our global simulations, they all suffer from the same limitations: they are axisymmetric and non time explicit. In the present paper, we have stressed the importance of treating the Jovian magnetosphere as nonaxisymmetric (see Figures 3–9, 12, and 13). The importance of the local time asymmetries in global MHD simulations of rotating magnetospheres was also emphasized recently by *Jia and Kivelson* [2016]. In addition, in situ measurements and remote sensing observations also highlighted the presence of strong local time asymmetries in the Jovian magnetosphere (see, for instance, *Khurana* [2001], *Krupp et al.* [2004], and *Radioti et al.* [2008]). Therefore, three-dimensional global MHD simulations can recover physics which is difficult to capture with the aforementioned analytical models, whereas the simplifications made in the aforementioned models do not allow them to predict the full auroral structures and the response to changing solar wind conditions.

Global MHD simulations also have drawbacks. First of all, they are of course limited by the physics included in the equations. Second, global simulations are limited by their numerical resolutions, and small-scale effects cannot be captured. Increasing the resolution is, for practical reasons, not always possible, since global MHD simulations of Jupiter's magnetosphere are extremely computing intensive. This is because the speed of the MHD waves can be remarkably high in some regions of the simulations and because the size of the magnetosphere compared to the radius of Jupiter is extremely large. Finally, as mentioned in Section 2, the numerical diffusion is usually larger than the physical diffusion in global MHD simulations, and better meshes should be used in order to decrease this diffusion (which would make the simulations even more computing intensive). Although numerical diffusion is an issue, it does not seem to affect our simulations drastically, since our results are in quantitative agreement with remote sensing observations, in situ measurements, and theoretical predictions of the transport properties.

7.2. Influence of the Solar Wind on the Main Oval

Our simulations demonstrate that an increase in the solar wind density results in a brightening of the main oval at Jupiter. We have shown that when the solar wind density increases from $\rho = 0.162$ amu cm^{-3} to $\rho = 1.104$ amu cm^{-3}, the total electrical current closing within Jupiter's ionosphere becomes 45% stronger. The magnetosphere needs several rotation periods to adjust to the new solar wind conditions, and the ionospheric currents need about 60 h to reach a new equilibrium. This correlation between the solar wind density and the brightness of the aurorae is in agreement with radio, infrared, ultraviolet, and X-ray observations.

We have shown in section 5 that the currents associated with the main oval in our simulations were overwhelmingly caused by the bent back of the field lines. We also showed that close to the equatorial plane,

it is much easier for subcorotating plasma to generate a strong azimuthal magnetic field (i.e., to generate bent back) on a elongated field line than on a compressed, more dipolar field line. Our simulations show (see Figure 2) that the denser the solar wind is, the more elongated the magnetic field lines are on the nightside. This is why stronger bent back is observed on the nightside when the solar wind density is high (see Figure 4), therefore generating more current and making the main auroral emission brighter.

On the dayside, on the other hand, the bent back of the field lines is modest (see Figure 4), which explains why the main oval is darker on the dayside. The modest bent back is the consequence of the field lines being more compressed on the dayside, making it more difficult for the subcorotating plasma to generate strong azimuthal magnetic field. In the simulations that we have performed, the density of the solar wind has almost no effect on the amount of bent back on the dayside (see Figure 4). This explains why the peak in the ionospheric field-aligned current is about the same for all simulations on the dayside (see Figure 8). Nevertheless, high solar wind density does influence the main oval on the dayside: it makes it broader (see Figure 7). This is simply because the field lines are more compressed on the dayside when the solar wind density is large. As a result, the same range of radial distances in the equatorial plane maps to a larger range of latitude in the ionosphere. The consequence is that the total amount of field-aligned currents flowing in the ionosphere on the dayside increases when the solar wind becomes denser (see Figure 9).

A larger solar wind ram pressure implies larger mechanical stresses on Jupiter's magnetosphere. These stresses generate larger magnetic and flow stresses within the magnetosphere, and the ionospheric currents necessary to counterbalance these stresses thus need to become stronger, producing brighter aurorae. This correlation between the solar wind density and the brightness of the aurorae was already observed many times in all available wave length (radio, infrared, ultraviolet, X-ray), see section 1. Nevertheless, theories [*Cowley and Bunce*, 2001; *Southwood and Kivelson*, 2001; *Cowley and Bunce*, 2003] predicted the opposite: that the main oval emission and the solar wind density should be anticorrelated. The idea is that an increase in solar wind ram pressure should push the plasma inward and then, because of the conservation of angular momentum, the plasma should be accelerated in the azimuthal direction, reducing the amount of subcorotation in the magnetosphere and therefore reducing the strength of the currents in the corotation enforcement current system (responsible for the main oval).

Our simulations show that this scenario is only happening on the dayside and that it only lasts a few hours (see Figure 11). Indeed, when the magnetopause moves inward (at the beginning of the simulations) the plasma is only pushed inward on the dayside, not on the nightside. In addition, the decrease of the ionospheric field-aligned currents responsible for the main oval on the dayside only lasts a few hours because once the magnetopause found a new equilibrium position, it does not push the plasma inward anymore, and the azimuthal velocity of the magnetospheric plasma does not increase any more.

8. Summary and Conclusions

In the present paper, using three-dimensional MHD simulations, we have studied the influence of the solar wind on the Jovian magnetosphere, in particular on the brightness of the main oval. We found that a high solar wind ram pressure enhances the asymmetries in the magnetosphere, even deep inside the magnetosphere. For instance, in our simulations, the magnetic field lines are elongated on the nightside and more compressed on the dayside. This day-night asymmetry is more pronounced when the solar wind ram pressure is high. We also found that the bent back of the magnetic field lines is more pronounced at dawn than at dusk. And again, an increase in solar wind ram pressure enhances this dawn-dusk asymmetry. The dusk-dawn asymmetry can also be seen in the plasma angular velocity: the plasma rotates faster at dawn than at dusk, especially when the solar wind ram pressure is high (in our simulations, at 30 R_J, the plasma rotates 2 times faster at dawn than at dusk for quiet solar wind conditions and 5.8 times faster at dawn than at dusk for very disturbed solar wind conditions). The ionospheric field-aligned currents responsible for the main auroral emission display a strong day-night asymmetry, with stronger currents on the nightside, and a light dawn-dusk asymmetry, with currents slightly stronger at dusk than at dawn. Like every other asymmetry in our simulations, it gets enhanced when the solar wind ram pressure is high.

Our simulations also show that the brightness of the main oval and the solar wind ram pressure are positively correlated. We additionally show that in our simulations, the electrical currents responsible for the main oval are overwhelmingly generated by the bent back of the magnetic field lines. On the nightside, the intensity

of the electric currents responsible for the main oval increases when the solar wind ram pressure is high. We found that this is because the field lines become more elongated, which tends to increase the azimuthal magnetic field responsible for the main oval. On the dayside, we found that the peak value of the main oval electrical currents is almost not affected by the solar wind ram pressure. But we also found that the main oval becomes broader and that consequently, the magnitude of the field-aligned currents flowing in the main oval integrated over all latitudes becomes larger. In our simulations, the main oval brightness slowly increased when the solar wind ram pressure was increased and needed about 60 h to adjust to the new solar wind conditions.

Our simulations are in agreement with observations, which consistently show that solar wind perturbations and aurorae brightness are positively correlated. JUNO in situ measurements, in the solar wind and in the magnetosphere, combined with remote sensing of Jupiter's aurora will be very helpful to better understand the detailed time evolution and associated local time asymmetries of Jupiter's auroral oval, and the response of variations in the solar wind.

Acknowledgments
E.C. was funded by the Research Foundation-Flanders (grant FWO 12M0115N). Computations were performed on the supercomputers Muk and ThinKing (provided by the VSC (Flemish Supercomputer Center), funded by the Research Foundation-Flanders (FWO) and the Flemish Government-department (EWI), as well as on Trillian (a Cray XE6m-200 supercomputer at the University of New Hampshire supported by the NSF MRI program under grant PHY-1229408). E.C. would also like to acknowledge the ISSI teams "Coordinated Numerical Modeling of the Global Jovian and Saturnian Systems" and "How does the Solar Wind Influence the Giant Planet Magnetospheres?" for useful discussions. The simulation data of this paper are available upon request.

References

Badman, S. V., et al. (2016), Weakening of Jupiter's main auroral emission during January 2014, *Geophys. Res. Lett.*, *43*, 988–997, doi:10.1002/2015GL067366.

Bagenal, F., and P. A. Delamere (2011), Flow of mass and energy in the magnetospheres of Jupiter and Saturn, *J. Geophys. Res. Space Physics*, *116*, A05209, doi:10.1029/2010JA016294.

Baron, R. L., T. Owen, J. E. P. Connerney, T. Satoh, and J. Harrington (1996), Solar wind control of Jupiter's H_3^+ auroras, *Icarus*, *120*, 437–442, doi:10.1006/icar.1996.0063.

Barrow, C. H. (1978), Jupiter's decametric radio emission and solar activity, *Planet. Space Sci.*, *26*, 1193–1199, doi:10.1016/0032-0633(78)90059-4.

Barrow, C. H. (1979), Association of corotating magnetic sector structure with Jupiter's decameter-wave radio emission, *J. Geophys. Res.*, *84*, 5366–5372, doi:10.1029/JA084iA09p05366.

Barrow, C. H., F. Genova, and M. D. Desch (1986), Solar wind control of Jupiter's decametric radio emission, *Astron. Astrophys.*, *165*, 244–250.

Bonfond, B., J. Gustin, J.-C. Gérard, D. Grodent, A. Radioti, B. Palmaerts, S. V. Badman, K. K. Khurana, and C. Tao (2015), The far-ultraviolet main auroral emission at jupiter—Part 1: Dawn-dusk brightness asymmetries, *Ann. Geophys.*, *33*(10), 1203–1209, doi:10.5194/angeo-33-1203-2015.

Caudal, G. (1986), A self-consistent model of Jupiter's magnetodisc including the effects of centrifugal force and pressure, *J. Geophys. Res.*, *91*, 4201–4221, doi:10.1029/JA091iA04p04201.

Chané, E., S. Poedts, and B. van der Holst (2008), On the combination of ACE data with numerical simulations to determine the initial characteristics of a CME, *Astron. Astrophys.*, *492*, L29–L32, doi:10.1051/0004-6361:200811022.

Chané, E., J. Saur, and S. Poedts (2013), Modeling Jupiter's magnetosphere: Influence of the internal sources, *J. Geophys. Res. Space Physics*, *118*, 2157–2172, doi:10.1002/jgra.50258.

Clarke, J. T., D. Grodent, S. W. H. Cowley, E. J. Bunce, P. Zarka, J. E. P. Connerney, and T. Satoh (2004), Jupiter's aurora, in *Jupiter: The Planet, Satellites and Magnetosphere*, edited by F. Bagenal, T. E. Dowling, and W. B. McKinnon, pp. 639–670, Cambridge Univ. Press., Cambridge.

Clarke, J. T., et al. (2009), Response of Jupiter's and Saturn's auroral activity to the solar wind, *J. Geophys. Res.*, *114*, A05210, doi:10.1029/2008JA013694.

Cowley, S. W. H., and E. J. Bunce (2001), Origin of the main auroral oval in Jupiter's coupled magnetosphere-ionosphere system, *Planet. Space Sci.*, *49*, 1067–1088.

Cowley, S. W. H., and E. J. Bunce (2003), Modulation of Jupiter's main auroral oval emissions by solar wind induced expansions and compressions of the magnetosphere, *Planet. Space Sci.*, *51*, 57–79.

Cowley, S. W. H., J. D. Nichols, and E. J. Bunce (2002), Distributions of current and auroral precipitation in Jupiter's middle magnetosphere computed from steady-state Hill-Pontius angular velocity profiles: Solutions for current sheet and dipole magnetic field models, *Planet. Space Sci.*, *50*, 717–734, doi:10.1016/S0032-0633(02)00046-6.

Dunn, W. R., et al. (2016), The impact of an ICME on the Jovian X-ray aurora, *J. Geophys. Res. Space Physics*, *121*, 2274–2307, doi:10.1002/2015JA021888.

Ebert, R., F. Bagenal, D. McComas, and C. Fowler (2014), A survey of solar wind conditions at 5 AU: A tool for interpreting solar wind-magnetosphere interactions at Jupiter, *Front. Astron. Space Sci.*, *1*, 4, doi:10.3389/fspas.2014.00004.

Echer, E., P. Zarka, W. D. Gonzalez, A. Morioka, and L. Denis (2010), Solar wind effects on Jupiter non-Io DAM emissions during Ulysses distant encounter (2003–2004), *Astron. Astrophys.*, *519*, A84, doi:10.1051/0004-6361/200913305.

Fukazawa, K., T. Ogino, and R. J. Walker (2006), Configuration and dynamics of the Jovian magnetosphere, *J. Geophys. Res. Space Physics*, *111*, A10207, doi:10.1029/2006JA011874.

Genova, F., P. Zarka, and C. H. Barrow (1987), Voyager and Nancay observations of the Jovian radio-emission at different frequencies—Solar wind effect and source extent, *Astron. Astrophys.*, *182*, 159–162.

Gurnett, D. A., et al. (2002), Control of Jupiter's radio emission and aurorae by the solar wind, *Nature*, *415*, 985–987.

Hendrix, T., R. Keppens, and P. Camps (2015), Modelling ripples in Orion with coupled dust dynamics and radiative transfer, *Astron. Astrophys.*, *575*, A110, doi:10.1051/0004-6361/201425498.

Hess, S. L. G., E. Echer, and P. Zarka (2012), Solar wind pressure effects on Jupiter decametric radio emissions independent of Io, *Planet. Space Sci.*, *70*, 114–125, doi:10.1016/j.pss.2012.05.011.

Hill, T. W. (1979), Inertial limit on corotation, *J. Geophys. Res.*, *84*, 6554–6558, doi:10.1029/JA084iA11p06554.

Hill, T. W. (2001), The Jovian auroral oval, *J. Geophys. Res.*, *106*, 8101–8108, doi:10.1029/2000JA000302.

Jia, X., and M. G. Kivelson (2016), Dawn-dusk asymmetries in rotating magnetospheres: Lessons from modeling Saturn, *J. Geophys. Res. Space Physics*, *121*, 1413–1424, doi:10.1002/2015JA021950.

Joy, S. P., M. G. Kivelson, R. J. Walker, K. K. Khurana, C. T. Russell, and T. Ogino (2002), Probabilistic models of the Jovian magnetopause and bow shock locations, *J. Geophys. Res.*, *107*(A10), 1309, doi:10.1029/2001JA009146.

Kaiser, M. L. (1993), Time-variable magnetospheric radio emissions from Jupiter, *J. Geophys. Res.*, *98*(18), 18,757–18,765, doi:10.1029/93JE01279.
Keppens, R., Z. Meliani, A. J. van Marle, P. Delmont, A. Vlasis, and B. van der Holst (2012), Parallel, grid-adaptive approaches for relativistic hydro and magnetohydrodynamics, *J. Comput. Phys.*, *231*, 718–744, doi:10.1016/j.jcp.2011.01.020.
Keppens, R., C. Xia, and O. Porth (2015), Solar prominences: "Double, double... boil and bubble", *Astrophys. J. Lett.*, *806*, L13, doi:10.1088/2041-8205/806/1/L13.
Khurana, K. K. (2001), Influence of solar wind on Jupiter's magnetosphere deduced from currents in the equatorial plane, *J. Geophys. Res.*, *106*, 25,999–26,016, doi:10.1029/2000JA000352.
Knight, S. (1973), Parallel electric fields, *Planet. Space Sci.*, *21*, 741–750, doi:10.1016/0032-0633(73)90093-7.
Krupp, N., et al. (2004), Dynamics of the Jovian magnetosphere, in *Jupiter: The Planet, Satellites and Magnetosphere*, edited by F. Bagenal, T. E. Dowling, and W. B. McKinnon, pp. 617–638, Cambridge Univ. Press., Cambridge, U. K.
Ladreiter, H. P., and Y. Leblanc (1989), Jovian hectometric radiation—Beaming, source extension, and solar wind control, *Astron. Astrophys.*, *226*, 297–310.
Meng, X., G. Tóth, M. W. Liemohn, T. I. Gombosi, and A. Runov (2012), Pressure anisotropy in global magnetospheric simulations: A magnetohydrodynamics model, *J. Geophys. Res.*, *117*, A08216, doi:10.1029/2012JA017791.
Miyoshi, T., and K. Kusano (1997), MHD simulation of a rapidly rotating magnetosphere interacting with the external plasma flow, *Geophys. Res. Lett.*, *24*, 2627–2630, doi:10.1029/97GL52739.
Monceau-Baroux, R., O. Porth, Z. Meliani, and R. Keppens (2015), The SS433 jet from subparsec to parsec scales, *Astron. Astrophys.*, *574*, A143, doi:10.1051/0004-6361/201425015.
Moriguchi, T., A. Nakamizo, T. Tanaka, T. Obara, and H. Shimazu (2008), Current systems in the Jovian magnetosphere, *J. Geophys. Res.*, *113*, A05204, doi:10.1029/2007JA012751.
Morioka, A., F. Tsuchiya, Y. Miyoshi, H. Misawa, H. Oya, and K. Furukawa (2002), Duration of Jovian magnetospheric disturbances inferred from decametric radio storms, *Earth, Planets, and Space*, *54*, 1277–1281.
Nichols, J., and S. Cowley (2004), Magnetosphere-ionosphere coupling currents in Jupiter's middle magnetosphere: Effect of precipitation-induced enhancement of the ionospheric Pedersen conductivity, *Ann. Geophys.*, *22*, 1799–1827, doi:10.5194/angeo-22-1799-2004.
Nichols, J. D. (2011), Magnetosphere-ionosphere coupling in Jupiter's middle magnetosphere: Computations including a self-consistent current sheet magnetic field model, *J. Geophys. Res.*, *116*, A10232, doi:10.1029/2011JA016922.
Nichols, J. D., and S. W. H. Cowley (2005), Magnetosphere-ionosphere coupling currents in Jupiter's middle magnetosphere: Effect of magnetosphere-ionosphere decoupling by field-aligned auroral voltages, *Ann. Geophys.*, *23*, 799–808, doi:10.5194/angeo-23-799-2005.
Nichols, J. D., E. J. Bunce, J. T. Clarke, S. W. H. Cowley, J.-C. Gérard, D. Grodent, and W. R. Pryor (2007), Response of Jupiter's UV auroras to interplanetary conditions as observed by the Hubble Space Telescope during the Cassini flyby campaign, *J. Geophys. Res. Space Physics*, *112*, A02203, doi:10.1029/2006JA012005.
Nichols, J. D., J. T. Clarke, J. C. Gérard, D. Grodent, and K. C. Hansen (2009), Variation of different components of Jupiter's auroral emission, *J. Geophys. Res.*, *114*, A06210, doi:10.1029/2009JA014051.
Nichols, J. D., N. Achilleos, and S. W. H. Cowley (2015), A model of force balance in Jupiter's magnetodisc including hot plasma pressure anisotropy, *J. Geophys. Res. Space Physics*, *120*(12), 10,185–10,206, doi:10.1002/2015JA021807.
Panchenko, M., H. O. Rucker, and W. M. Farrell (2013), Periodic bursts of Jovian non-Io decametric radio emission, *Planet. Space Sci.*, *77*, 3–11, doi:10.1016/j.pss.2012.08.015.
Pontius, D. H. (1997), Radial mass transport and rotational dynamics, *J. Geophys. Res.*, *102*, 7137–7150, doi:10.1029/97JA00289.
Pontius, D. H. Jr., and T. W. Hill (1982), Departure from corotation of the Io plasma torus—Local plasma production, *Geophys. Res. Lett.*, *9*, 1321–1324, doi:10.1029/GL009i012p01321.
Porth, O., C. Xia, T. Hendrix, S. P. Moschou, and R. Keppens (2014), MPI-AMRVAC for solar and astrophysics, *Astrophys. J.*, *214*, 4, doi:10.1088/0067-0049/214/1/4.
Prangé, R., L. Pallier, K. C. Hansen, R. Howard, A. Vourlidas, R. Courtin, and C. Parkinson (2004), An interplanetary shock traced by planetary auroral storms from the Sun to Saturn, *Nature*, *432*, 78–81, doi:10.1038/nature02986.
Pryor, W. R., et al. (2005), Cassini UVIS observations of Jupiter's auroral variability, *Icarus*, *178*, 312–326, doi:10.1016/j.icarus.2005.05.021.
Radioti, A., J. Gérard, D. Grodent, B. Bonfond, N. Krupp, and J. Woch (2008), Discontinuity in Jupiter's main auroral oval, *J. Geophys. Res.*, *113*, A01215, doi:10.1029/2007JA012610.
Ray, L. C., Y.-J. Su, R. E. Ergun, P. A. Delamere, and F. Bagenal (2009), Current-voltage relation of a centrifugally confined plasma, *J. Geophys. Res.*, *114*, A04214, doi:10.1029/2008JA013969.
Ray, L. C., R. E. Ergun, P. A. Delamere, and F. Bagenal (2010), Magnetosphere-ionosphere coupling at Jupiter: Effect of field-aligned potentials on angular momentum transport, *J. Geophys. Res.*, *115*, A09211, doi:10.1029/2010JA015423.
Saur, J., B. H. Mauk, A. Kaßner, and F. M. Neubauer (2004), A model for the azimuthal plasma velocity in Saturn's magnetosphere, *J. Geophys. Res.*, *109*, A05217, doi:10.1029/2003JA010207.
Southwood, D. J., and M. G. Kivelson (2001), A new perspective concerning the influence of the solar wind on the Jovian magnetosphere, *J. Geophys. Res.*, *106*, 6123–6130, doi:10.1029/2000JA000236.
Tanaka, T. (1994), Finite volume TVD scheme on an unstructured grid system for three-dimensional MHD simulation of inhomogeneous systems including strong background potential fields, *J. Comput. Phys.*, *111*, 381–390, doi:10.1006/jcph.1994.1071.
Tao, C., H. Fujiwara, and Y. Kasaba (2010), Jovian magnetosphere-ionosphere current system characterized by diurnal variation of ionospheric conductance, *Planet. Space Sci.*, *58*, 351–364, doi:10.1016/j.pss.2009.10.005.
Terasawa, T., K. Maezawa, and S. Machida (1978), Solar wind effect on Jupiter's non-Io-related radio emission, *Nature*, *273*, 131–132, doi:10.1038/273131a0.
Tóth, G. (1996), A general code for modeling MHD flows on parallel computers: Versatile advection code, *Astrophys. Lett. Commun.*, *34*, 245–250.
van der Holst, B., S. Poedts, E. Chané, C. Jacobs, G. Dubey, and D. Kimpe (2005), Modelling of solar wind, CME initiation and CME propagation, *Space Sci. Rev.*, *121*, 91–104, doi:10.1007/s11214-006-6541-7.
Walker, R. J., and T. Ogino (2003), A simulation study of currents in the Jovian magnetosphere, *Planet. Space Sci.*, *51*, 295–307.
Walker, R. J., T. Ogino, and M. G. Kivelson (2001), Magnetohydrodynamic simulations of the effects of the solar wind on the Jovian magnetosphere, *Planet. Space Sci.*, *49*, 237–245.
Went, D. R., M. G. Kivelson, N. Achilleos, C. S. Arridge, and M. K. Dougherty (2011), Outer magnetospheric structure: Jupiter and Saturn compared, *J. Geophys. Res.*, *116*, A04224, doi:10.1029/2010JA016045.

Woch, J., N. Krupp, A. Lagg, and A. Tomás (2004), The structure and dynamics of the Jovian energetic particle distribution, *Adv. Space Res.*, *33*, 2030–2038, doi:10.1016/j.asr.2003.04.050.

Zarka, P., and F. Genova (1983), Low-frequency Jovian emission and solar wind magnetic sector structure, *Nature*, *306*, 767–768, doi:10.1038/306767a0.

Zieger, B., K. C. Hansen, T. I. Gombosi, and D. L. De Zeeuw (2010), Periodic plasma escape from the mass-loaded Kronian magnetosphere, *J. Geophys. Res.*, *115*, A08208, doi:10.1029/2009JA014951.